



Metalloporphyrin conjugated porous polymer in-situ grown on a Celgard separator as multifunctional polysulfide barrier and catalyst for high-performance Li-S batteries

Xin Guan^a, Yajun Zhao^a, Huijie Pei^a, Maoji Zhao^a, Yong Wang^a, Xingping Zhou^{a,*}, Mohamed Gamal Mohamed^{b,c}, Shiao-Wei Kuo^b, Yunsheng Ye^{b,*}

^a School of Chemistry and Chemical Engineering, Huazhong University of Science and Technology, Wuhan 430074, PR China

^b Department of Materials and Optoelectronic Science, National Sun Yat-sen University, Kaohsiung 80424, Taiwan

^c Department of Chemistry, Faculty of Science, Assiut University, Assiut 71515, Egypt

ARTICLE INFO

Keywords:

Conjugated porous polymer
Poly-metal-porphyrin
Catalysis
Li-S batteries

ABSTRACT

The severe shuttling of soluble polysulfides (LiPSs) (Li_2S_x , $4 \leq x \leq 8$) and sluggish kinetics of solid–solid conversion ($\text{Li}_2\text{S}_2 \rightarrow \text{Li}_2\text{S}$), lead to the premature end of discharge, resulting in fast capacity decay, limiting the practical performance and safety of lithium-sulfur batteries (LSBs). Functional modifiers on separators exhibit significant performances in migrating diffusion and promoting conversion for LiPSs; thus, endowing the separator with multiple high-performance parameters by multifactorial engineering to address the two issues mentioned above is an urgent need. Herein, for the first time, an ultra-light ($\approx 0.14 \text{ mg cm}^{-2}$) and multifunctional modifier consisting of metalloporphyrin conjugated porous polymer (Al-CPP) is interface-induced growth on the commercial separator to develop advanced LSBs. The electrocatalyst of metalloporphyrin is covalently constructed by an imidazolium-containing linker with bis(trifluoromethane)sulfonimide (TFSI^-) anions within the porous skeleton, improving diffusion and conversion of LiPSs as well as facilitating electrolyte accessibility and Li^+ transport, thereby performing enhanced full-range sulfur redox kinetics, and guiding uniform Li deposition. The in-situ growth of metalloporphyrin conjugated porous polymer is further verified in LSBs that realize superior rate performances and long lifespans. This contribution proposes an efficient in-situ growth of an ultra-light modifier design strategy to functionalize separators and inspires multi-function synergetic integration facing high-performance LSBs.

1. Introduction

Owing to their high theoretical specific capacity (1675 mAh g^{-1}), energy density (2600 Wh kg^{-1}), natural abundance, and low cost, lithium-sulfur batteries (LSBs) are an appealing candidate for high energy-density batteries [1]. However, the rapid capacity degradation, low Coulombic efficiency, and cycling instability originating from the dissolution and migration of soluble lithium polysulfides (LiPSs) (Li_2S_x , $4 \leq x \leq 8$) described as the “shuttle effect” has become the most prominent problem in LSBs. Moreover, the LiPS shuttling becomes severe by the sluggish kinetics of multi-electron reactions through solid–liquid–solid–solid phase transformation ($\text{S}_8 \rightarrow \text{Li}_2\text{S}_4 \rightarrow \text{Li}_2\text{S}_2 \rightarrow \text{Li}_2\text{S}$) of the S-cathode during the discharging process, leading to an inferior rate capability [2]. To meet intractable challenges in the marketization

process of LSBs, a promising strategy to inhibit the shuttle effect through rational engineering of separators with effective LiPS trapping and transformation abilities remains a critical issue in LSBs.

In recent years, strenuous efforts have been pursued to mitigate the shuttle effect by coating/or filtrating the functional material, such as carbon-based materials (e.g., carbon spheres [3], carbon nanotubes [4], graphene [5]), metal oxides (e.g., MoO_3 [6], ZnO [7], Al_2O_3 [8]), metal sulfides (e.g., ZnS [9], MoS_2 [10], CoS [11]) and metal–organic frameworks (MOFs) [12–14], on the commercial polyolefin separator facing the S-cathode. Due to their polar groups, the surface-modified layer composed by functional materials has significantly improved electrolyte affinity, Li-ion distribution, and LiPS inhibition. Among them, transition metal oxides (e.g., CoO [15], Nb_2O_5 [16], TiO_2 [17]) as modified layers exhibit many properties that are conducive to mutual

* Corresponding authors.

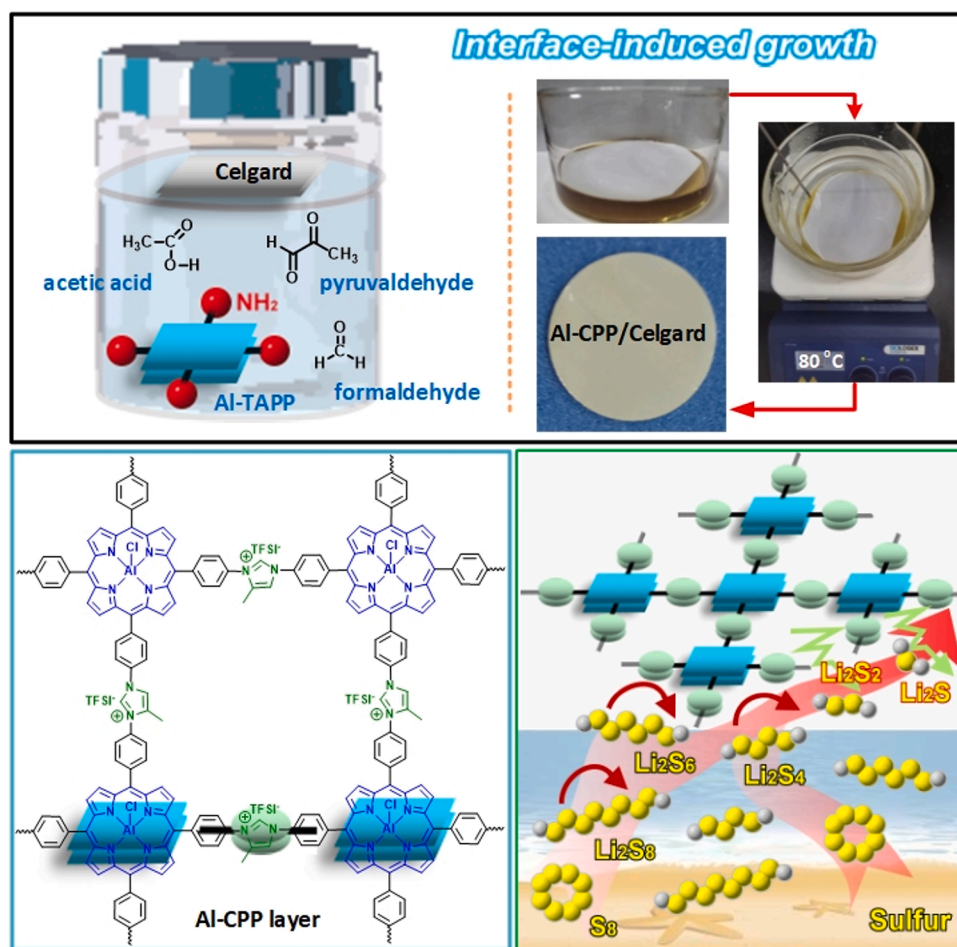
E-mail addresses: xpzhou@hust.edu.cn (X. Zhou), ysye@mail.nsysu.edu.tw (Y. Ye).

<https://doi.org/10.1016/j.cej.2023.144733>

Received 4 April 2023; Received in revised form 12 June 2023; Accepted 9 July 2023

Available online 10 July 2023

1385-8947/© 2023 Published by Elsevier B.V.



Scheme 1. The stepwise fabrication process of the Al-CPP *in-situ* functionalized separator.

conversion between soluble long-chain (Li_2S_x , $4 \leq x \leq 8$) and insoluble short-chain (Li_2S_2 , Li_2S) LiPSs, which effectively inhibit LiPS shuttle but also accelerate the reaction kinetics, thus obtaining excellent cycling performance. To achieve functionalization of separators, slurry casting and vacuum assistant filtration (VAF) as facile and practical approaches have been proposed and employed to prepare modified separators [18]. Nevertheless, these modified separators still suffer from falling Li-ion conduction or low efficiency for suppressing LiPS diffusion caused by too dense or loose structure for their modified layers. In addition, the thickness and weight of various designed modified separators are usually much more significant than those of commercial separators, which would apparently reduce the transport of Li ions and decrease the overall energy density of LSBs. So far, only rarely are findings presented that obtained functional separators with significant enhancement in LiPS trapping and transformation abilities through a more effective strategy for achieving high-rate and long-cycle-life LSBs. For instance, a MOF-derived Co_9S_8 nanowall array with vertical hollow nano-architecture and high electrical conductivity was *in-situ* grown on a Celgard *via* an interface-induced approach as a multifunctional polar barrier (mass loading of $\approx 0.16 \text{ mg cm}^{-2}$), enhancing the performance of LSBs [19]. Another MOF-derived $\text{Ni}_3(\text{HITP})_2$ ($\text{HITP} = 2,3,6,7,10,11$ -hexaiminotriphenylene) has been demonstrated that the *in-situ* growth microporous modified layer on Celgard with low mass loading ($\approx 0.066 \text{ mg cm}^{-2}$), favorable absorption capacity for LiPSs, and high conductivity can significantly improve performance LSBs [20]. Besides, the double-sided nano brick-wall structure, constructed by MoS_2 /poly diallyl dimethyl ammonium chloride (PDDA) hybrid in conjunction with polyacrylic acid (PAA), was fabricated *via* layer-by-layer (LBL) self-assembly approach, showing ultralight loading of modified layer

(0.10 mg cm^{-2}), excellent LiPSs trapping and Li dendrite suppressing for achieving outstanding cycle stability [21]. In this regard, it is meaningful to design a novel functional separator, which can be very thin for fast ion transport and offer effective active sites to physically/chemically trap and catalyze LiPSs for high electrochemical utilization.

Porphyrin compounds are ubiquitous and perform essential functions of life, which have been widely investigated as catalysts in various fields due to their unique 2D and $18 e^-$ conjugate structures. Specifically, the molecular electrocatalytic active sites are constructed to form the conjugated porous polymer (CPP) that affords a stable and necessary interspace and allows easy accessibility of reactants and their media, thereby ensuring effective electrocatalytic reaction [22]. Despite their numerous electrocatalytic features, the synthesized CPPs are usually in the form of solid-state, thus lacking sufficient homogeneity for molecular sieving applications. Therefore, the controllable fabrication of continuous large-area CPP membranes with small thicknesses and optimal pore size is significant in porphyrin application and helps create high-performance LSBs. Herein, the *in-situ* growth of a large-area, ultra-thin, consistent, and microporous layer on Celgard has been reported using a metalloporphyrin conjugated porous polymer by tetra-(4-aminophenyl)porphyrin aluminum (Al-TAPP). For the first time, it has been demonstrated that the metalloporphyrin conjugated porous polymer modifier can be simultaneously used as the barrier and catalyzer for LiPS in designing high-performance LSBs. Scheme 1 shows that the Al single-atom catalyst coordinated CPP (Al-CPP) with an extremely low mass loading of $\approx 0.14 \text{ mg cm}^{-2}$ can be directly produced on the Celgard surface using a facile interface-induced growth approach. The forming imidazolium-containing linker with bis(trifluoromethane)sulfonimide (TFSI^-) anions not only integrates the metalloporphyrin active sites but

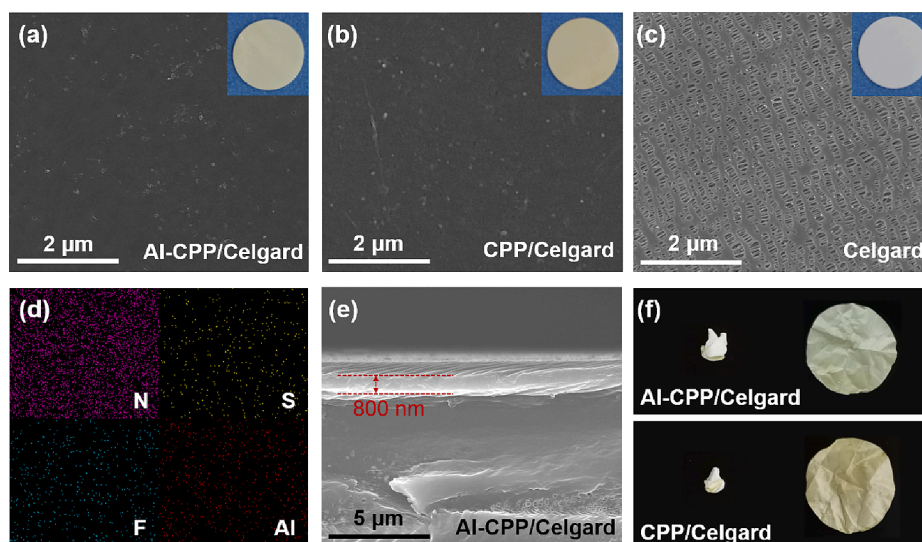


Fig. 1. SEM of the top surfaces of (a) Al-CPP/Celgard, (b) CPP/Celgard, and (c) Celgard. (d) The corresponding EDX mapping of Al-CPP/Celgard. (e) SEM of the cross-sectional surface of Al-CPP/Celgard. (f) Photographs of Al-CPP/Celgard and CPP/Celgard after folding.

also facilitates electrolyte affinity and Li-ions transport for the LSBs' separator. The as-designed Al-CPP layer endows the separator with chemical/physical adsorption for LiPSs, enhances full-range sulfur redox kinetics, and guides uniform Li deposition. As a result, LSBs based on Al-CPP functionalized Celgard (Al-CPP/Celgard) delivered stable sulfur electrochemistry, high rate performance, long cycling lifespan, and competitive areal capacity under high sulfur loading. The *in-situ* growth strategy represents insight into the rational construct of metalloporphyrin-conjugated porous polymer toward advanced LSBs.

2. Experimental section

2.1. Preparation of Al-CPP/Celgard and CPP/Celgard

Celgard separators were first oxidized by KHSO_5 (10 wt% in deionized water) at $80\text{ }^\circ\text{C}$ for 1.5 h. Put the oxidized Celgard in the deionized water (120 mL) solution of Al-TAPP (8.9 μmol), glacial acetic (0.5 mL), formaldehyde (35.6 μmol) and pyruvaldehyde (35.6 μmol), and heated to $80\text{ }^\circ\text{C}$ for 8 h. Then, the separators were put in LiTFSI solution (100 mL, 1 wt% in deionized water) at room temperature and stirred for 2 h, and vacuum dried at $60\text{ }^\circ\text{C}$ to get Al-CPP/Celgard. Replacing Al-TAPP with TAPP and reacting similarly to get CPP/Celgard. The preparation of Al-TAPP and TAPP are showed in supporting information [23,24].

2.2. Battery assembly

The S-cathode, separator (modified layer facing S-cathode), electrolyte, and Li metal of the battery were assembled into 2032-type coin cells. The electrolyte was 1 M LiTFSI salt in a solvent mixture of DME and DOL (1:1 v/v) with 1% LiNO_3 additive. The cathode was prepared of S, CB, and PVDF at a ratio of 6:3:1 coating on Al foil. The active material loading in the S-cathode was $\approx 1\text{ mg cm}^{-2}$ (diameter 12 mm) and $\approx 3.0\text{ mg cm}^{-2}$ (diameter 10 mm).

2.3. Symmetric battery

The C-cathode, separator with Li_2S_6 electrolyte, and C-cathode of the symmetric battery were assembled into 2032-type coin cells. The Li_2S_6 electrolyte (saturated) was prepared by the overnight reaction of Li_2S and S in a molar ratio of 1:5 in the electrolyte. The C-cathode was prepared of CB and PVDF at a ratio of 8:2 coating on Al foil. The CB loading in the C-cathode was $\approx 1\text{ mg cm}^{-2}$ (diameter 12 mm).

3. Results and discussion

The stepwise fabrication process of the Al-CPP *in-situ* functionalized separators is schematically illustrated in Scheme 1, along with photographs. The *in-situ* modifier is composed of the micro-porous porphyrin for physically blocking lithium polysulfides (LiPSs) and imidazolium-containing linker with (TFSI⁻) anions for facilitating Li-ions transport. Among metal elements, Al is the third most abundant element and the most abundant metal on Earth. It is also widely used because it is lightweight, easily recyclable, and stable against corrosion. In Al coordinated Por, the Al center is ready to form Lewis acid-base adduct with an incoming base, which can be regarded as one of the most accessible and unique single-atom catalysts for Li-S batteries [25]. The modifier's precursor (TAPP) was transferred to Al ion-centered TAPP (Al-TAPP) through the metalation of Al salt. Then, the CPP with and without Al ion was grown *in-situ* on the Celgard through a facile solution method, which allows scalable production of the Al-CPP/Celgard and CPP/Celgard, respectively (Fig. S1). It is noted that the color of the oxidized Celgard is wholly changed to light yellow after the solution reaction at $80\text{ }^\circ\text{C}$, suggesting the *in-situ* polymerization of Al-CPP (or CPP) on the Celgard surface. The morphology of the resulting separators was further characterized by scanning electron microscopy (SEM) (Fig. 1), showing that *in-situ* polymerized CPPs uniformly covered an irregular porous of the pristine Celgard. The energy-dispersive X-ray spectroscopy (EDX) mapping confirms the uniform distribution of N, S, F, and Al elements through the Al-CPP/Celgard (Fig. 1d). The thickness and weight of the *in-situ* growth layer on the Celgard are critical parameters in designing high-energy-density LSBs. An ultra-thin ($>800\text{ nm}$) and ultra-light ($>0.14\text{ mg cm}^{-2}$) Al-CPP modified layer attached to the surface of Celgard is visible in the cross-sectional SEM images (Fig. 1e), which is much thicker than most modified separators by blade-coating and filtration approaches ($>10\text{ }\mu\text{m}$). Besides, modified CPP and Al-CPP layers are firmly attached to the Celgard surface through *in-situ* polymerization, evidenced by no stripped and cracked samples after repeated folding and unfolding (Fig. 1f). The XRD pattern further presents the transformation of the crystalline structure of TAPP to the amorphous structure for the polymerized CPP powder (Fig. S2). Besides, the Brunauer-Emmett-Teller (BET) surface area analysis indicates the synthesized CPP contains prolific mesopores identified as type-IV isotherms with type H3 hysteresis loops, which can be determined to be the specific surface area of $280\text{ m}^2\text{ g}^{-1}$ (Fig. S3), which could provide more active sites and 3D diffusion channels to achieve effective physical or

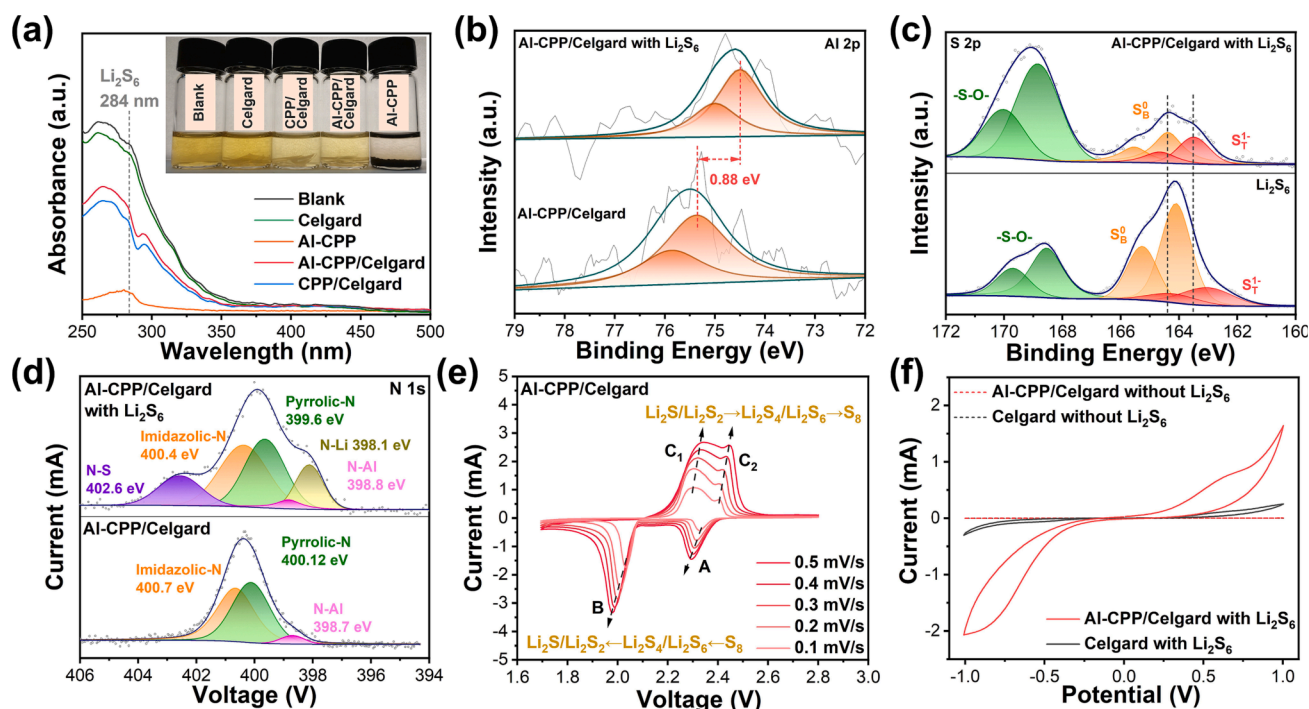


Fig. 2. (a) UV-vis spectra and the photographs of the LiPSs solutions before and after adsorbed adding CPP; (b) Al 1 s, (c) S 2p, (d) N 1 s XPS spectra of Al-CPP/Celgard before and after adsorption of LiPSs; (e) CV curves of cell with Al-CPP/Celgard at different scan rates; (f) CV curves of added Li_2S_6 symmetrical cells with Celgard, CPP/Celgard, and Al-CPP/Celgard.

chemical LiPS adsorption and fast Li-ion conduction, respectively.

Initially, Fourier transform infrared spectroscopy (FTIR) of the TAPP and Al-TAPP are depicted in Fig. S4, showing characteristic absorption peaks of the pyrrole ring at $\approx 1510\text{ cm}^{-1}$ and $-\text{NH}_2$ at ≈ 3449 and $\approx 3372\text{ cm}^{-1}$ corresponding to porphyrin macro-ring and amino group, respectively. In Fig. S5 of $^1\text{H NMR}$, the proton signals at 8.88, 7.84, and 6.99 ppm are assigned to the hydrogen atom of the porphyrin macro-ring, and the peak at 5.58 ppm is ascribed to the amino group in the spectra of TAPP. After the metallation of Al salt, the peak at -2.74 ppm assigned to pyrrolic H ($-\text{NH}-$) in the porphyrin ring disappeared, indicating complete metallization with the Al cation. It can also be seen that the Al-TAPP shows the characteristic structure of the amino group at 149.0 ppm in $^{13}\text{C NMR}$ spectra (Fig. S6); and that the polymerized Al-TAPP (Al-CPP) presents specific signals at about 171.1, 137.7, and 148.8 ppm after being covalently bonded by imidazolium rings with TFSI anions, respectively. The X-ray photoelectron spectroscopy (XPS) spectra in Fig. S7 further characterized the obtained Al-CPP/Celgard, exhibiting two distinct peaks at 398.3 and 400.3 eV, which are related to the contribution of the Al-N bonds in the porphyrin ring and the C-N bonds in the imidazolium ring, respectively. Additionally, the presence of values of F 1s, S 2s, and S 2p at around 685.1, 230.0, and 166.3 eV, respectively, assigned to the TFSI $^-$ anion suggests that the CH_3COO^- in the imidazolium ring was ion-exchanged by LiTFSI salt, which strongly supports the new peaks at 1580, 1059 and 1202 cm^{-1} corresponding to the imidazolium ring, S=O and $-\text{CF}_3$ groups observed by FTIR analysis (Fig. S4). Therefore, these observations provide direct proof for the successful *in-situ* growth of the functional layer consisting of the porous polymer, Al metal active center, heterocyclic ring, and imidazolium-based linker, which can be reasonably expected to facilitate electrolyte infiltration, diffusion of Li^+ -ions, physical/chemical barrier and catalytic conversion for LiPS.

To evaluate the ability of the *in-situ* growth porphyrin-based CPP to adsorb LiPSs, the visualized adsorption test was carried out by adding the synthesized Al-CPP powder and Al-CPP/Celgard to the solution of LiPSs. Subsequently, the absorbances of the solutions after standing for 24 h were recorded using a UV-vis spectrophotometer (Fig. 2a). The

pristine Li_2S_6 solution was decolorized after adding Al-CPP powder, reflecting the excellent physical/chemical adsorption ability toward LiPSs by the imidazolium linker and porphyrin conjugated porous polymer. Due to its ultra-light modified layer, the Al-CPP/Celgard shows no apparent color change in the resultant Li_2S_6 solution but a weaker peak intensity at $\approx 285\text{ nm}$. To further verify the enhanced trapping ability toward LiPSs by porphyrin-based modifiers, XPS was conducted to investigate the chemical interaction between the Al-CPP (or CPP) and Li_2S_6 before and after adsorption. After interacting with Li_2S_6 , the binding energy of the Al 2p spectra of Al-CPP/Celgard exhibited a negative shift of 0.88 eV compared to that of the Al-CPP/Celgard as a result of the chemical interaction between Al and S (Fig. 2b). Electrons tend to be transferred from S atoms of Li_2S_6 to unsaturated Al atoms of Al-CPP/Celgard in the form of Lewis-base interactions [26]. For the XPS analysis of S 2p, the overall S 2p peaks exhibited a positive shift, revealing weaker electron cloud density by the electron transfer from S to Al atoms (Fig. 2c and Fig. S8a) [27]. Besides, the presence of two new peaks at 398.1 and 402.6 eV in the N 1s spectrum of adsorbed Li_2S_6 separator suggests the formation of the N-Li and N-S, respectively (Fig. 2d and Fig. S8b) [28,29]. These observations revealed that the simultaneous chemical bands Al-S, N-Li, and N-S could enhance the interaction between the modified Al-CPP layer and LiPSs, which is beneficial for the chemical inhibiting the shuttle effect. The interception function from Al-CPP was also examined by the permeation behavior of Li_2S_6 solution in an H-type cell separated by the separator. As shown in Fig. S9, the pure electrolyte in the inserted Celgard H-cell apparently turns to deep yellow within 1 h, while it can stay colorless after 24 h by inserting modified separators. The result also reflects that the porous structure is cooperative binding to form a dense LPS-barrier layer that can effectively inhibit the shuttle effect, therefore protecting the Li dendrite growth and passivation of the Li anode.

To demonstrate the structural benefit of the Al-CPP separator for facilitating the capability of accommodating and utilizing LiPSs, a series of electrochemical characterizations was performed. The liquid electrolyte uptake (EU) was first tested as 80%, 117%, and 124% for Celgard, CPP/Celgard, and Al-CPP/Celgard, respectively, illustrating a

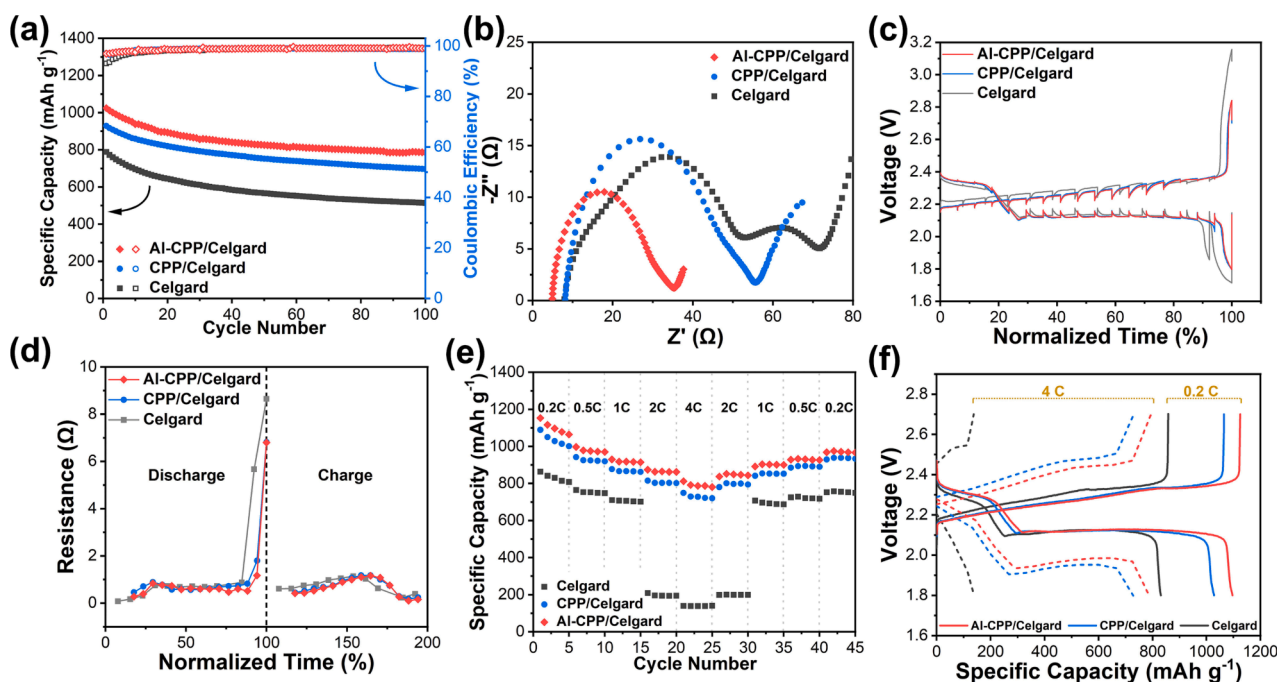


Fig. 3. (a) Cycling performance, (b) Nyquist plots, (c) GITT potential profiles recorded at 0.05 C, (d) resistance recorded as a function of normalized time of cells with Celgard, CPP/Celgard, and Al-CPP/Celgard, (e) rate-performance; (f) voltage profile curves.

limited enhancement in EU by additional modification due to the ultralight modified layer. However, the contact angles between the electrolyte and separator displayed 44.8° , 28.1° , and 22.6° for Celgard, CPP/Celgard, and Al-CPP/Celgard, respectively (Fig. S10). The porphyrin-modified layer's porous and lithiophilic polymer structure in CPP/Celgard and Al-CPP/Celgard separators accounted for improving electrolyte affinity, facilitating electrolyte infiltration and Li-ion diffusion. The improved electrolyte affinity is reflected in the ion-conductivity (σ) of the modified separators, showing a slightly higher σ value of 0.51 mS cm^{-1} than Celgard of 0.30 mS cm^{-1} . (Fig. S11) In LSB's cyclic voltammograms (CV) with the separators, two reduction peaks (peak A and B) and a border oxidation peak (peak C₁ and C₂) appear at ≈ 2.3 , ≈ 2.0 , and $\approx 2.4 \text{ V}$, corresponding to the two-step reduction of $\text{cyclo-S}_8 \rightarrow \text{Li}_2\text{S}_4\text{-}_8 \rightarrow \text{Li}_2\text{S}_2/\text{Li}_2\text{S}$ and reversible oxidation of $\text{Li}_2\text{S}_2/\text{Li}_2\text{S} \rightarrow \text{cyclo-S}_8$, respectively (Fig. 2e and Fig. S12) [30]. It can be observed that the cell with Al-CPP/Celgard displays much sharper and higher current peaks than those of CPP/Celgard and Celgard assembled cells, implying a quicker conversion between sulfur and LiPSs. Moreover, the CV profile displays a positive shift in reduction peaks and a negative shift in oxidation peaks as well as an increased Li diffusion coefficient (D_{Li^+}) calculated by the Randles-Sevcik equation (Fig. S12 and Table S1). The result illustrates that the cell with Al-CPP/Celgard exhibits a lower polarization, faster Li^+ diffusion, and redox kinetics, which can be expected to improve the cells' cycling performance and sulfur utilization by modifying the porphyrin-based conjugated porous polymer, especially after coordination with Al. Herein, the catalytic and kinetics effect of Al-CPP on sulfur-based conversion reaction was further studied by symmetric cells. As depicted in Fig. 2f, the CV tests were performed at 10 mV s^{-1} within a voltage range from -1.0 to 1.0 V . Notably, the peak current density of cells with Al-CPP presented a high peak current density manifesting the evident promotion of the liquid–solid heterogeneous redox reaction on Al-CPP during the charge/discharge processes [31]. Linear sweep voltammetry (LSV) exhibits electrochemical stability windows that the disintegrated potential of Al-CPP/Celgard is at about 4.7 V , more stable than Celgard (Fig. S13).

The barrier and catalytic effects of the Al-CPP modifier are further investigated by the charging/discharging behavior at a current rate of 0.5 C . After 100 cycles (Fig. 3a), the cells assembled with Al-CPP show

higher discharge capacity than CPP/Celgard and Celgard assembled cells (1024.3 vs. 928.5 and 788.6 mAh g^{-1} , respectively). In addition, the electrochemical impedance spectroscopy (EIS) and galvanostatic intermittent titration technique (GITT) measurements at a 0.05 C further demonstrate the function of Al-CPP on kinetic behavior. As shown in Fig. 3b, the EIS curves are presented in the form of Nyquist plots, where the semicircle at high frequency and inclined line at low frequency represent charge-transfer resistance (R_{ct}) and diffusion impedance of Li-ion, respectively. After the cycling, all cells revealed a similar semicircle at the high frequency and an inclined line at the low frequency, corresponding to charge transfer resistance (R_{ct}) and Warburg impedance (W), respectively. Besides, there was a new semicircle at the middle frequency of the cell with Celgard, representing the electrolyte/electrode interface resistance (R_{se}), caused by the shuttle of LiPSs. Obviously, the Al-CPP assembled cell exhibited a smaller R_{ct} value (27Ω) than that of CPP/Celgard (40Ω) and Celgard (48Ω) and unobservable semicircle in the medium-frequency area, indicating the lower charge-transfer resistance and limited LiPS diffusion of LSBs with Al-CPP/Celgard, which is in favor of kinetics [32]. The GITT profiles (Fig. 3c) were carried out by applying a constant current (I_{applied}) for 1 h to obtain the closed-circuit voltages (CCV), followed by a resting step in the absence of current for another 2 h to acquire the quasi-open-circuit-voltage (QOCV) and the internal resistance ($\Delta R_{\text{internal}}$) can be calculated by the equation: $\Delta R_{\text{internal}} (\Omega) = |\Delta V_{\text{QOCV-CCV}}| / I_{\text{applied}}$ in lithiation/delithiation process of LSBs. As shown in Fig. 3d, it was obvious that the $\Delta R_{\text{internal}}$ of the cell with modified separators is much lower than those of Celgard at both stages of LiPSs to $\text{Li}_2\text{S}_2/\text{Li}_2\text{S}$ in the discharge process and $\text{Li}_2\text{S}_2/\text{Li}_2\text{S}$ to LiPSs in charge process. The lower R_{internal} indicates the decreased reaction barrier by *in-situ* growth Al-CPP, leading to the faster redox kinetics of LiPSs with much-alleviated polarization [33,34].

As the rate performance is another essential factor for evaluating the electrochemical reaction kinetics, the rate performance of LSBs with the separators at various current densities was recorded. As depicted in Fig. 3e, the cell with Celgard delivered an initial discharge capacity of 863.2 mAh g^{-1} at 0.2 C and significantly dropped to $< 200 \text{ mAh g}^{-1}$ at $\geq 2.0 \text{ C}$. Furthermore, when the current rate abruptly switched back to 0.2 C , the specific capacity limitary recovered to 752.1 mAh g^{-1} , revealing poor reversibility at various current rates. However, at the

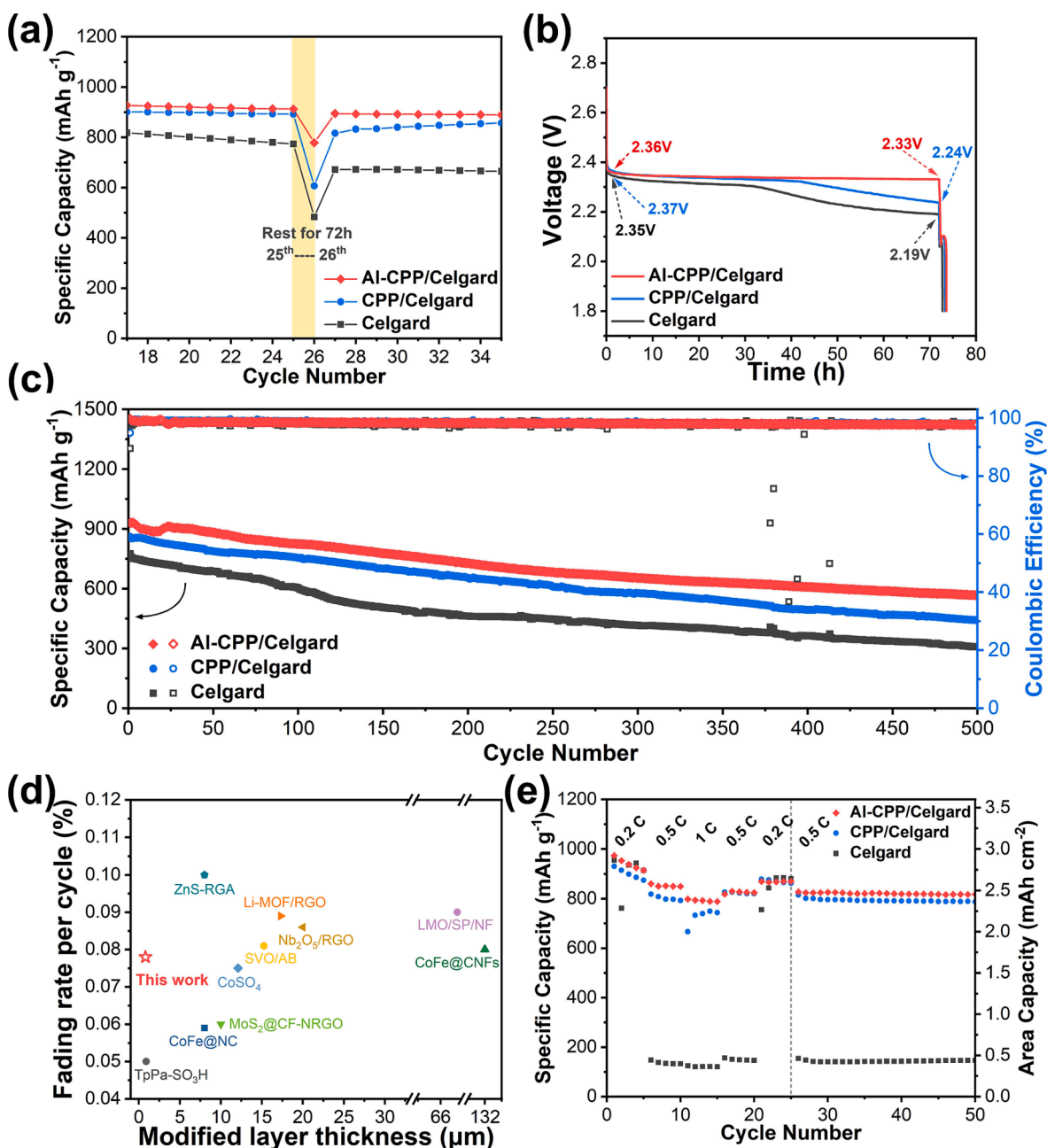


Fig. 4. (a) Self-discharge capacity and (b) potential-time curves of cells with Celgard, CPP/Celgard, and Al-CPP/Celgard during the interruption and rest processes; (c) long cycling performances of cells with Celgard, CPP/Celgard, and Al-CPP/Celgard; (d) comparison of fading rate per cycle and modified layer thickness between our work and selected results of LSBs with modified separators reported in the literature; (e) high-sulfur loading performances.

same range of current rates, the rate performances of the cells with both modified separators are less inferior to that of Celgard-assembled cells. The cell with Al-CPP/Celgard not only delivered an initial capacity of 1153.3 mAh g⁻¹ at 0.2 C but a discharge capacity of 812.0 mAh g⁻¹ at a high current density of 4.0 C, which is approximately 5.8 times higher than those of Celgard at 4.0 C. The cells' voltage profile curves in Fig. 3f and S14 display that the cells with modified separators are able to hold flat plateaus at all rates, while the plateau entirely disappears for the cell with Celgard at ≥ 2.0 C. Besides, the cells' potential gaps (ΔV) between charge and discharge plateaus at 50% discharge capacities also exhibit better electrochemical performance evidenced by minor ΔV in both modified separators assembled cells.

Self-discharge is another indicator of polysulfide shuttling level in Li-S batteries. The cells' self-discharge properties were evaluated by the set processes: (i) charging/discharging for 25 cycles at 0.5 C, (ii) charging to

2.7 V and resting for 72 h, (iii) discharging to 1.8 V, and subsequent charging/discharging for another 25 cycles at 0.5 C, which are essential criteria to determine LiPS diffusion during the resting period. As shown in Fig. 4a and 4b, the cell with Al-CPP/Celgard had the most negligible capacity loss of 134.0 mAh g⁻¹ and a loss rate of 14.7% compared with the discharge capacity of the 25th cycle ($Q_{26\text{th}} = 778$ mAh g⁻¹), as well as the highest capacity retention of 98% ($Q_{27\text{th}}/Q_{25\text{th}}$) and voltage retention of 2.3 V and after 72 h rest. Such results evidently indicate that the Al-CPP/Celgard can significantly mitigate the shuttle effect through the strong chemical/physical anchoring ability for LiPSs and accelerate the redox kinetics of LiPSs in the liquid phase. To meet the requirements for practical application, the long-term and high-sulfur loading performances of LSBs assembled with Al-CPP/Celgard are also investigated at a current density of 1.0 C. As shown in Fig. 4c, the Celgard assembled cell still suffered from a fast capacity degradation with 40%

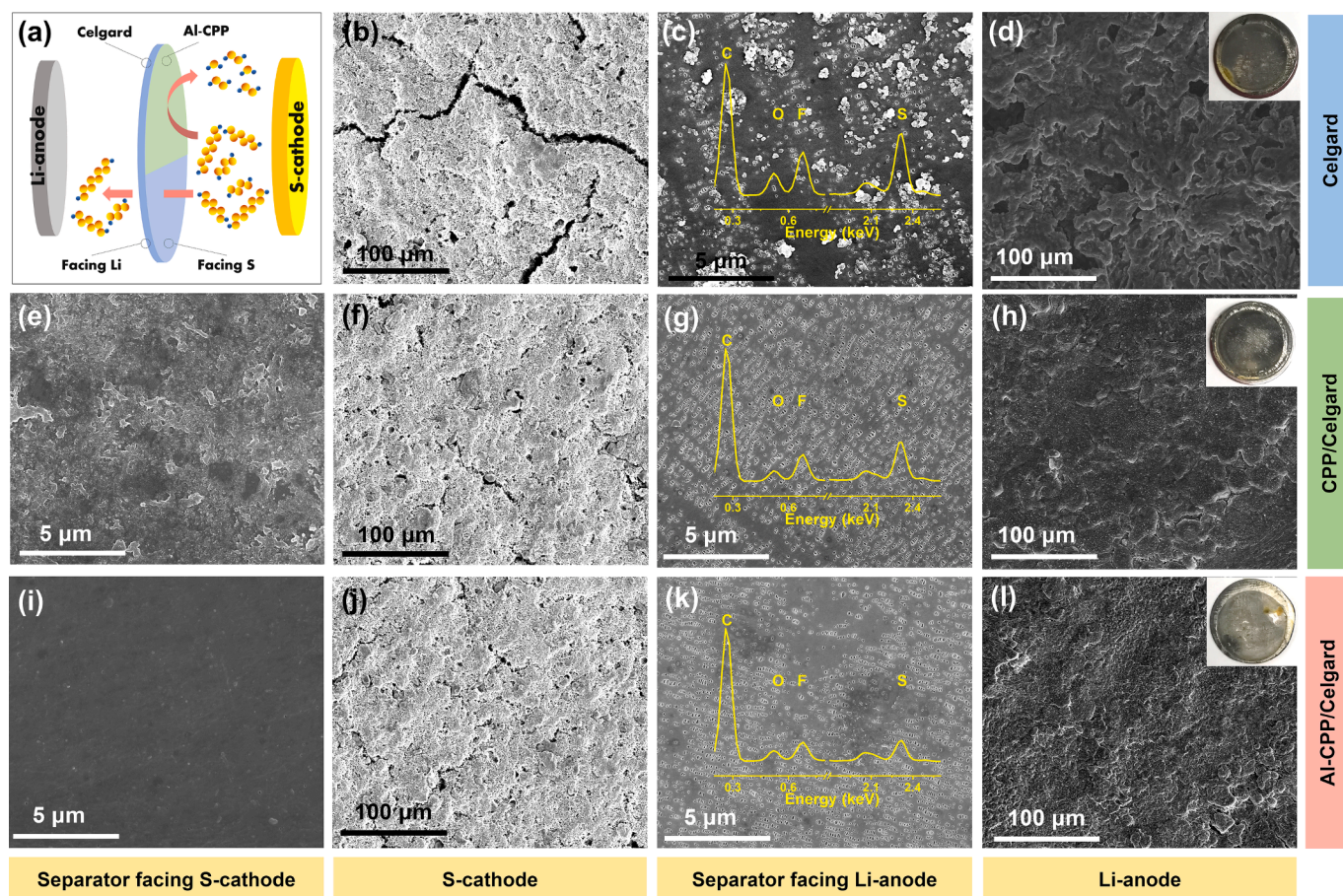


Fig. 5. (a) Schematic diagram. SEM images of the separators facing S-cathodes, the S-cathodes, the separators facing Li-anodes, and the Li-anodes of (b, c, d) Celgard, (e, f, g, h) CPP/Celgard, and (i, j, k, l) Al-CPP/Celgard after 100 cycles at 0.5 C.

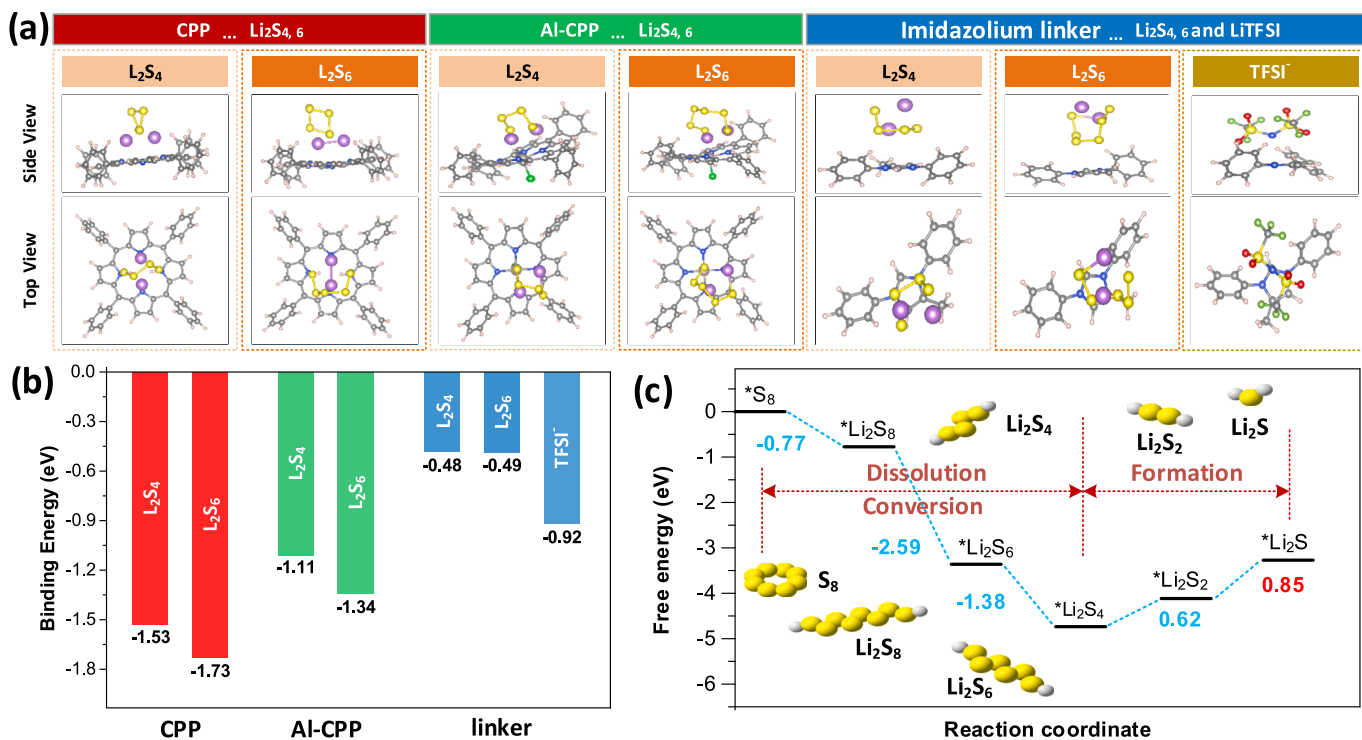


Fig. 6. (a) Optimized adsorption conformations of intermediate species on CPP, Al-CPP, and imidazolium linker. (b) Comparison of adsorption energies between $\text{Li}_2\text{S}_{4,6}$ and CPP, Al-CPP, and imidazolium linker. (c) Energy profiles for the reaction of Li_2S_n on Al-CPP; the potential limiting step is marked in red.

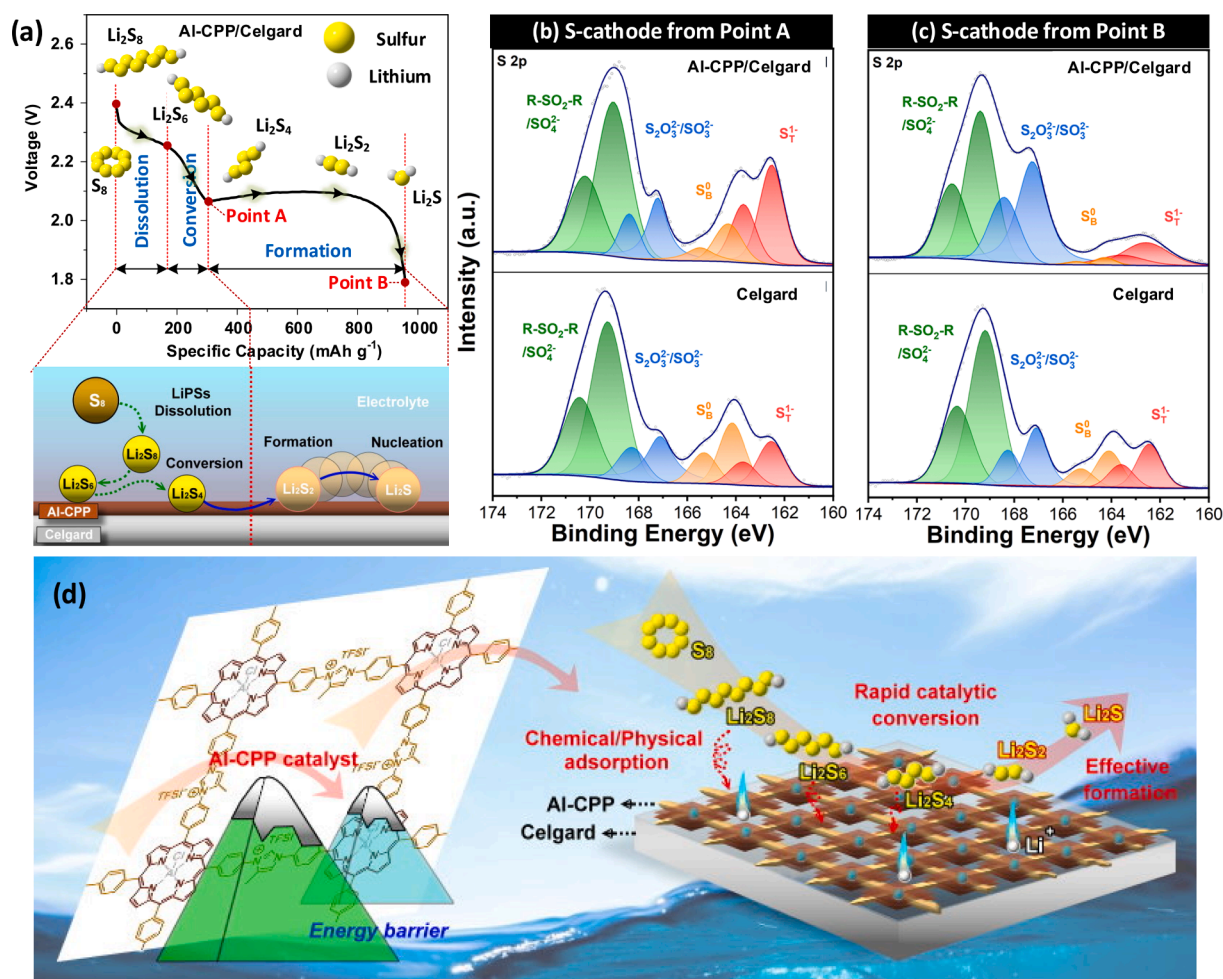


Fig. 7. (a) Schematic illustration of discharge profile with sulfur and various lithiation product configurations in different reaction regimes. XPS analysis of the discharge products collected from cycled S-cathode at (b) Point A and (c) Point B. (d) Schematic illustration of the reaction process of sulfur on the Al-CPP/Celgard separator.

capacity retention after 500 cycles and a high decay rate of 0.12% per cycle, indicative of severe shuttling of LiPSs. A significantly enhanced cycling stability was realized by employing Al-CPP/Celgard, with a high capacity of 566.7 mAh g^{-1} after 500 cycles, corresponding to 61% of the initial capacity and 0.078% of the decay rate per cycle, which is considered more stable than the recently reported LSBs with modified separators at a much lower modified layer thickness of 800 nm (Fig. 4d and Table S2). With rising sulfur loading to $> 3.0 \text{ mg cm}^{-2}$, an initial discharge capacity of 973.7 mAh g^{-1} was achievable at 0.2 C (Fig. 4e). After 100 cycles, it can retain a high capacity of 826.8 mAh g^{-1} at 0.5 C, but the cell with Celgard occurred severe polarization. The high-loading electrode also shows superb cycling stability, indicating it holds significant promises for high-performance LSBs owing to the synergistic effect of a strong shuttle barrier and catalytic conversion for LiPSs.

To get insights into the performance enhancement of LSB by Al-CPP/Celgard, the cells with Celgard and modified separators were disassembled after 100 cycles, and the S-cathode, separator, and Li-anode were retrieved and examined by SEM and digital photographs (Fig. 5). As shown in Fig. 5b, the S-cathode facing pristine Celgard suffered from severe suttling with apparent cracks on the surface. The cycled Celgard-facing Li-anode surface is covered with many irregular particles that should be derived from the deposition of dissolved LiPSs and dead Li. The EDX mapping also shows an apparent peak intensity in the S element, indicative of severe LiPS shuttling from the S-cathode (Fig. 5c). Simultaneously, severe corrosion occurred on the surface of Li-anode, which turned black with noticeable dendrite growth (Fig. 5d). In

contrast, a more uniform and intact surface of both S-cathode (Fig. 5f and 5j) and Li-anode (Fig. 5h and 5l) was observed in the SEM images with CPP and Al-CPP/Celgard. With modified separators, no visible particles and low S element for the separator surface facing the Li-anode, suggesting that the in-situ formed CPP and Al-CPP could prohibit the shuttling of LiPS and protect the Li-anode (Fig. 5g and 5k). What's more, the separators facing S-cathodes were observed that Al-CPP and CPP layers still complete and uniform on the surface, confirming Al-CPP and CPP layers are very stable during the cycling (Fig. 5e and 5i).

To understand the catalytic mechanism of Al-CPP at the atomic level, the first-principle calculation based on density functional theory (DFT) was further performed. DFT calculations were first carried out to investigate the interaction between soluble LiPSs of Li_2S_4 , Li_2S_6 and porphyrin-based modifiers. As shown in Fig. 6a and 6b, the optimized binding configuration between the Li_2S_4 , Li_2S_6 and CPP with/without Al revealed that the S and Li atoms of Li_2S_4 , Li_2S_6 with the N atom of CPP as well as N and Al atoms of Al-CPP, and corresponding binding energies (E_b) are -1.53 , -1.73 and -1.11 , -1.34 eV, respectively, demonstrating that porphyrin molecule structure with/without Al possesses the more vital anchoring ability for LiPSs [35,36]. Moreover, the imidazolium linker in synthesized CPP and Al-CPP also exhibited the binding energies to LiPSs as well as TFSI, indicating improved anchoring and dissociation abilities for LiPSs and Li salt by the typical feature of imidazolium bonding, respectively [21]. Additionally, Gibbs free energies have also been estimated for S reduction on Al-CPP substrate from S_8 to Li_2S (Fig. 6c). It

is noted that the Al-CPP shows the spontaneous exothermic conversion from S_8 to Li_2S_4 , which may result from the excellent adsorption of S and Li atoms and lead to high accessibility and transformation of the intermediates. The following two steps to form Li_2S_2 and Li_2S are endothermic, which possess the positive Gibbs free energy of 0.62 and 0.85 eV in the thermodynamic process. The later step is generally treated as the rate-limiting step in the whole discharging process, and the value for Li_2S_2 to LiS formation step is similar to or even less than the other reported active materials, showing that the reduction of S is thermodynamically more favorable on *in-situ* Al-CPP [37,38].

To further demonstrate the catalytic effect of Al-CPP on improving the conversion of LiPSs, the cycled S-cathode from the disassembled cells with Celgard, and Al-CPP/Celgard at "Point A" and "Point B" in Fig. 7a are investigated by XPS. For the cells at both points, the peaks located at 169.3 and 167.1 eV are assigned to R-SO₂-R/SO₄²⁻ and S₂O₃²⁻/SO₃²⁻, respectively, resulting from the oxidization of sulfur species during sample transfer or the residual LiTFSI. S 2p spectra of the S-cathode at point A (Fig. 7b) show two unique components corresponding to bridging sulfur (S_B^0) and terminal sulfur (S_T^0) at 163.9 and 162.5 eV in the sulfur/or LiPSs, respectively. It can be seen that the peak area ratio of S_T^0 to S_B^0 (S_T^0/S_B^0) in Celgard (0.78) significantly raised to 2.61 by modifying Al-CPP, showing more short-chain LiPSs produced with Al-CPP assistance during the liquid-liquid transition process. Besides, Al-CPP is also helpful for converting Li_2S_2 to Li_2S , evidenced by much lower S_T^0/S_B^0 in Al-CPP/Celgard assembled cells (7.11) than Celgard (1.23) (Fig. 7c). Based on these observations, the multi-function mechanism of the *in-situ* growth Al-CPP is illustrated in Fig. 7d. Typically, the S_8 is firstly transformed into long-chain LiPSs, such as Li_2S_6 and Li_2S_4 , and dissolved in the electrolyte during the liquid-liquid transition process. The *in-situ* growth Al-CPP has a superior confining ability toward the dissolved LiPSs via chemical/physical adsorption, avoids shuttling through the separator, and promotes the electrolyte accessibility for the improvements of reduction S_8 . Subsequently, the long-chain LiPSs are further reduced to solid Li_2S_2 . Due to the lower dissociation energy of Li_2S_2 on the surface of Al-CPP, the nucleation and growth of Li_2S_2 become more effective and easier, resulting in fast redox kinetics and high sulfur utilization during long-term charge-discharge processes.

4. Conclusion

In summary, we designed and synthesized a large-area, ultra-thin, consistent Al-CPP via the *in-situ* polymerization of Al-TAPP on the Celgard surface. The surface-modified metalloporphyrin conjugated porous polymer enables efficient inhibiting of soluble LiPSs shuttle and enhances the full-range sulfur redox kinetics in LSBs. Taking synergistic advantages of the chemical/physical confinement of LiPSs by CPP's skeleton and facilitated Li^+ diffusion by the imidazolium-containing linker and porous structure, shuttling LiPSs was effectively alleviated, promising high reaction kinetics and stable cycling performance. More importantly, the catalytic capability of the CPP modifiers could be optimized by inserting the Al-ion into its conjugated structure to further improve the electrochemical performance of LSBs. As a result, exceptional electrochemical performance was demonstrated for LSBs with high rate performance, long cycling lifespan, and competitive areal capacity under high sulfur loading, which outperforms most of the reported modified separators. In conclusion, our study offered a practical method for modifying standard polyolefin separators with conjugated porous polymer to prevent polysulfide shuttle and accelerate polysulfide conversion, and open a new way to modify separators for solving the shuttling and low redox kinetics challenges of LiPSs and promote the practical application of LSBs. On the basis of this work, a novel class of CPP with a single-atom catalyst will be synthesized by a simple post-modification and utilized in the future as a functionalized layer on the separator for high performance Li-S batteries, thereby rationalizing the entire production process and making it more accessible.

Declaration of Competing Interest

The authors declare that they have no known competing financial interests or personal relationships that could have appeared to influence the work reported in this paper.

Data availability

Data will be made available on request.

Acknowledgments

We acknowledge financial support from the National Natural Science Foundation of China (52020105012) and analytical and testing assistance from the Analysis and Testing Center of HUST.

Appendix A. Supplementary data

Supplementary data to this article can be found online at <https://doi.org/10.1016/j.cej.2023.144733>.

References

- [1] S. Li, W. Zhang, J. Zheng, M. Lv, H. Song, L. Du, Inhibition of polysulfide shuttles in Li-S batteries: modified separators and solid-state electrolytes, *Adv. Energy Mater.* 11 (2) (2020) 2000779, <https://doi.org/10.1002/aenm.202000779>.
- [2] P. Wang, B. Xi, M. Huang, W. Chen, J. Feng, S. Xiong, Emerging catalysts to promote kinetics of lithium-sulfur batteries, *Adv. Energy Mater.* 11 (7) (2021) 2002893, <https://doi.org/10.1002/aenm.202002893>.
- [3] H. Liao, H. Zhang, H. Hong, Z. Li, Y. Lin, Novel flower-like hierarchical carbon sphere with multi-scale pores coated on PP separator for high-performance lithium-sulfur batteries, *Electrochim. Acta* 257 (2017) 210–216, <https://doi.org/10.1016/j.electacta.2017.10.069>.
- [4] W. Tian, B. Xi, H. Mao, J. Zhang, J. Feng, S. Xiong, Systematic exploration of the role of a modified layer on the separator in the electrochemistry of lithium-sulfur batteries, *ACS Appl. Mater. Interfaces* 10 (36) (2018) 30306–30313, <https://doi.org/10.1021/acsami.8b08438>.
- [5] X. Ou, Y. Yu, R. Wu, A. Tyagi, M. Zhuang, Y. Ding, I.H. Abidi, H. Wu, F. Wang, Z. Luo, Shuttle suppression by polymer-sealed graphene-coated polypropylene separator, *ACS Appl. Mater. Interfaces* 6 (6) (2018) 5534–5542, <https://doi.org/10.1021/acsami.7b17251>.
- [6] N. Kaisar, S.A. Abbas, J. Ding, H.A. Chen, C.W. Pao, K.M. Boopathi, A. Mohapatra, Y.T. Chen, S.H. Wu, J. Fang, S. Jou, C.W. Chu, A lithium passivated MoO₃ nanobellet decorated polypropylene separator for fast-charging long-life Li-S batteries, *Nanoscale* 11 (6) (2019) 2892–2900, <https://doi.org/10.1039/c8nr08262f>.
- [7] N. Shi, B. Xi, Z. Feng, F. Wu, D. Wei, J. Liu, S. Xiong, Insight into different-microstructured zn/graphene-functionalized separators affecting the performance of lithium-sulfur batteries, *J. Mater. Chem. A* 7 (8) (2019) 4009–4018, <https://doi.org/10.1039/c8ta12409d>.
- [8] R. Song, R. Fang, L. Wen, Y. Shi, S. Wang, F. Li, A trilayer separator with dual function for high performance lithium-sulfur batteries, *J. Power Sources* 301 (2016) 179–186, <https://doi.org/10.1016/j.jpowsour.2015.10.007>.
- [9] Z. Liu, Z. Hu, X. Jiang, Y. Zhang, X. Wang, S. Zhang, Multi-functional ZnS quantum dots/graphene aerogel modified separator for high performance lithium-sulfur batteries, *Electrochim. Acta* 422 (2022), 140496, <https://doi.org/10.1016/j.electacta.2022.140496>.
- [10] J. Wu, H. Zeng, X. Li, H. Pei, Z. Xue, Y.S. Ye, X. Xie, Dual-functional interlayer based on radially oriented ultrathin mo₂s nanosheets for high-performance lithium-sulfur batteries, *ACS Appl. Energy Mater.* 2 (3) (2019) 1702–1711, <https://doi.org/10.1021/acsami.8b01805>.
- [11] Y. Yang, S. Wang, L. Zhang, Y. Deng, H. Xu, X. Qin, G. Chen, CoS-interposed and ketjen black-embedded carbon nanofiber framework as a separator modulation for high performance Li-S batteries, *Chem. Eng. J.* 369 (2019) 77–86, <https://doi.org/10.1016/j.cej.2019.03.034>.
- [12] C. Song, G. Li, Y. Yang, X. Hong, S. Huang, Q. Zheng, L. Si, M. Zhang, Y. Cai, 3D catalytic MOF-based nanocomposite as separator coatings for high-performance Li-S battery, *Chem. Eng. J.* 381 (2020), 122701, <https://doi.org/10.1016/j.cej.2019.122701>.
- [13] H. Chen, Y. Xiao, C. Chen, J. Yang, C. Gao, Y. Chen, J. Wu, Y. Shen, W. Zhang, S. Li, F. Huo, B. Zheng, Conductive MOF-modified separator for mitigating the shuttle effect of lithium-sulfur battery through a filtration method, *ACS Appl. Mater. Interfaces* 11 (12) (2019) 11459–11465, <https://doi.org/10.1021/acsami.8b22564>.
- [14] M. Tian, F. Pei, M. Yao, Z. Fu, L. Lin, G. Wu, G. Xu, H. Kitagawa, X. Fang, Ultrathin MOF nanosheet assembled highly oriented microporous membrane as an interlayer for lithium-sulfur batteries, *Energy Storage Mater.* 21 (2019) 14–21, <https://doi.org/10.1016/j.ensm.2018.12.016>.
- [15] H. Li, Y. Wang, H. Chen, B. Niu, W. Zhang, D. Wu, Synergistic mediation of polysulfide immobilization and conversion by a catalytic and dual-adsorptive

- system for high performance lithium-sulfur batteries, *Chem. Eng. J.* 406 (2021), 126802, <https://doi.org/10.1016/j.cej.2020.126802>.
- [16] P. Guo, K. Sun, X. Shang, D. Liu, Y. Wang, Q. Liu, Y. Fu, D. He, Nb₂O₅/RGO nanocomposite modified separators with robust polysulfide traps and catalytic centers for boosting performance of lithium-sulfur batteries, *Small* 15 (40) (2019) e1902363.
- [17] L. Jiao, C. Zhang, C. Geng, S. Wu, H. Li, W. Lv, Y. Tao, Z. Chen, G. Zhou, J. Li, G. Ling, Y. Wan, Q.H. Yang, Capture and catalytic conversion of polysulfides by in situ built TiO₂-MXene heterostructures for lithium-sulfur batteries, *Adv. Energy Mater.* 9 (19) (2019) 1900219, <https://doi.org/10.1002/aenm.201900219>.
- [18] M. Chen, M. Shao, J. Jin, L. Cui, H. Tu, X. Fu, Configurational and structural design of separators toward shuttling-free and dendrite-free lithium-sulfur batteries: a review, *Energy Storage Mater.* 47 (2022) 629–648, <https://doi.org/10.1016/j.ensm.2022.02.051>.
- [19] J. He, Y. Chen, A. Manthiram, Vertical Co₉S₈ hollow nanowall arrays grown on a celgard separator as a multifunctional polysulfide barrier for high-performance Li-S batteries, *Energy Environ. Sci.* 11 (9) (2018) 2560–2568, <https://doi.org/10.1039/c8ee00893k>.
- [20] Y. Zang, F. Pei, J. Huang, Z. Fu, G. Xu, X. Fang, Large-area preparation of crack-free crystalline microporous conductive membrane to upgrade high energy lithium-sulfur batteries, *Adv. Energy Mater.* 8 (31) (2018) 1802052, <https://doi.org/10.1002/aenm.201802052>.
- [21] J. Wu, H. Zeng, X. Li, X. Xiang, Y. Liao, Z. Xue, Y. Ye, X. Xie, Ultralight layer-by-layer self-assembled MoS₂-polymer modified separator for simultaneously trapping polysulfides and suppressing lithium dendrites, *Adv. Energy Mater.* 8 (35) (2018) 1802430, <https://doi.org/10.1002/aenm.201802430>.
- [22] P. Gao, Z. Chen, Z. Zhao-Karger, J.E. Mueller, C. Jung, S. Klyatskaya, T. Diemant, O. Fuhr, T. Jacob, R.J. Behm, M. Ruben, M. Fichtner, A porphyrin complex as a self-conditioned electrode material for high-performance energy storage, *Angew Chem Int Ed Engl* 56 (35) (2017) 10341–10346, <https://doi.org/10.1002/anie.201702805>.
- [23] Y. Wang, Y. Zhao, Y. Ye, H. Peng, X. Zhou, X. Xie, X. Wang, F. Wang, A One-Step Route to CO₂-Based Block Copolymers by Simultaneous ROCOP of CO₂/Epoxides and RAFT Polymerization of Vinyl Monomers, *Angew Chem Int Ed* 57 (14) (2018) 3593–3597, <https://doi.org/10.1002/anie.201710734>.
- [24] M. Zhao, S. Zhu, X. Yang, Y. Wang, X. Zhou, X. Xie, A porphyrinic donor-acceptor conjugated porous polymer as highly efficient photocatalyst for PET-RAFT polymerization, *Macromol Rapid Commun* 43 (18) (2022) e2200173.
- [25] N. Zarrabi, P.K. Poddutoori, Aluminum(III) porphyrin: a unique building block for artificial photosynthetic systems, *Coord. Chem. Rev.* 429 (2021), 213561, <https://doi.org/10.1016/j.ccr.2020.213561>.
- [26] J. Huang, B. Cao, F. Zhao, L. Zhang, Y. Qu, Y. Chen, A Mulberry-like Hollow Carbon Cluster Decorated by Al-doped ZnO Particles for Advanced Lithium-Sulfur Cathode, *Electrochim. Acta* 304 (2019) 62–69, <https://doi.org/10.1016/j.electacta.2019.02.082>.
- [27] Y. Tian, G. Li, Y. Zhang, D. Luo, X. Wang, Y. Zhao, H. Liu, P. Ji, X. Du, J. Li, Z. Chen, Low-Bandgap Se-Deficient Antimony Selenide as a Multifunctional Polysulfide Barrier toward High-Performance Lithium-Sulfur Batteries, *Adv. Mater.* 32 (4) (2020) e1904876.
- [28] P. Zhang, M. Li, B. Yang, Y. Fang, X. Jiang, G.M. Veith, X.G. Sun, S. Dai, Polymerized Ionic Networks with High Charge Density: Quasi-Solid Electrolytes in Lithium-Metal Batteries, *Adv. Mater.* 27 (48) (2015) 8088–8094, <https://doi.org/10.1002/adma.201502855>.
- [29] L. Zhang, X. Chen, F. Wan, Z. Niu, Y. Wang, Q. Zhang, J. Chen, Enhanced Electrochemical Kinetics and Polysulfide Traps of Indium Nitride for Highly Stable Lithium-Sulfur Batteries, *ACS Nano* 12 (9) (2018) 9578–9586, <https://doi.org/10.1021/acsnano.8b05466>.
- [30] Q. Tang, Z. Shan, L. Wang, X. Qin, K. Zhu, J. Tian, X. Liu, Nafion coated sulfur-carbon electrode for high performance lithium-sulfur batteries, *J. Power Sources* 246 (2014) 253–259, <https://doi.org/10.1016/j.jpowsour.2013.07.076>.
- [31] X. Yang, X. Gao, Q. Sun, S.P. Jand, Y. Yu, Y. Zhao, X. Li, K. Adair, L.Y. Kuo, J. Rohrer, J. Liang, X. Lin, M.N. Banis, Y. Hu, H. Zhang, X. Li, R. Li, H. Zhang, P. Kaghazchi, T.K. Sham, X. Sun, Promoting the Transformation of Li₂S₂ to Li₂S: significantly increasing utilization of active materials for high-sulfur-loading Li-S batteries, *Adv. Mater.* 31 (25) (2019) e1901220.
- [32] Q.X. Shi, H.J. Pei, N. You, J. Wu, X. Xiang, Q. Xia, X.L. Xie, S.B. Jin, Y.S. Ye, large-scaled covalent triazine framework modified separator as efficient inhibit polysulfide shuttling in Li-S batteries, *Chem. Eng. J.* 375 (2019), 121977, <https://doi.org/10.1016/j.cej.2019.121977>.
- [33] X. Yang, S. Chen, W. Gong, X. Meng, J. Ma, J. Zhang, L. Zheng, H.D. Abruna, J. Geng, Kinetic Enhancement of Sulfur Cathodes by N-Doped Porous Graphitic Carbon with Bound VN Nanocrystals, *Small* 16 (48) (2020) e2004950.
- [34] J. Park, E.T. Kim, C. Kim, J. Pyun, H.-S. Jang, J. Shin, J.W. Choi, K. Char, Y.-E. Sung, The importance of confined sulfur nanodomains and adjoining electron conductive pathways in subreaction regimes of Li-S Batteries, *Adv. Energy Mater.* 7 (19) (2017) 1700074, <https://doi.org/10.1002/aenm.201700074>.
- [35] S. Hu, M. Yi, X. Huang, D. Wu, B. Lu, T. Wang, N. Li, Z. Zhu, X. Liu, J. Zhang, Cobalt-doped porphyrin-based porous organic polymer-modified separator for high-performance lithium-sulfur batteries, *J. Mater. Chem. A* 9 (5) (2021) 2792–2805, <https://doi.org/10.1039/d0ta10607k>.
- [36] X. Song, F. Zhou, M. Yao, C. Hao, J. Qiu, Insights into the anchoring of polysulfides and catalytic performance by metal phthalocyanine covalent organic frameworks as the cathode in lithium-sulfur batteries, *ACS Sustainable Chem. Eng.* 8 (27) (2020) 10185–10192, <https://doi.org/10.1021/acssuschemeng.0c02563>.
- [37] Z. Du, X. Chen, W. Hu, C. Chuang, S. Xie, A. Hu, W. Yan, X. Kong, X. Wu, H. Ji, L. J. Wan, Cobalt in nitrogen-doped graphene as single-atom catalyst for high-sulfur content lithium-sulfur batteries, *J. Am. Chem. Soc.* 141 (9) (2019) 3977–3985, <https://doi.org/10.1021/jacs.8b12973>.
- [38] B. Yu, A. Huang, K. Srinivas, X. Zhang, F. Ma, X. Wang, D. Chen, B. Wang, W. Zhang, Z. Wang, J. He, Y. Chen, Outstanding Catalytic Effects of 1T'-MoTe₂ Quantum Dots@3D Graphene in Shuttle-Free Li-S Batteries, *ACS Nano* 15 (8) (2021) 13279–13288, <https://doi.org/10.1021/acsnano.1c03011>.